Enhancement of nanoparticle formation and growth during the COVID-19 lockdown period in urban Beijing

Xiaojing Shen[1,*], Junying Sun[1], Fangqun Yu[2]~~, Xiaoye Zhang[1]~~, Ying Wang[1], Junting Zhong[1,3], Yangmei Zhang[1], Xinyao Hu[1], Can Xia[1,4], Sinan Zhang[1], Xiaoye Zhang[1]

5 1 State Key Laboratory of Severe Weather & Key Laboratory of Atmospheric Chemistry of CMA, Chinese Academy of Meteorological Sciences, Beijing 100081, China

2 Atmospheric Sciences Research Center, State University of New York at Albany, 251 Fuller Road, Albany, New York 12203, USA

3 University of Chinese Academy of Sciences, Beijing 100049, China

10 4 Nanjing University of Information Science & Technology, Nanjing 210000, China

Correspondence to: Xiaojing Shen (shenxj@cma.gov.cn)

Abstract. Influenced by the spread of the global 2019 novel coronavirus (COVID-19) pandemic, primary emissions of particles and precursors associated with anthropogenic activities decreased significantly in China during the Chinese New Year of 2020 and the lockdown period (January 24–February 16, 2020)~~, as indicated by approximately 50% reduction of NO_x~~

15 ~~emission nation wide based on the open literature~~. Two-month measurements of the number size distribution of neutral particles and charged ions showed that during the lockdown (LCD) period, the number concentration of particles smaller than 100 nm decreased by approximately 40% compared to the ~~pre~~Pre -LCD period in January. However, the accumulation mode particles increased by approximately 20% as several polluted episodes contributed to secondary aerosol formation. In this study, new particle formation (NPF) events were found to be enhanced in the nucleation and growth processes during the LCD

20 period, as indicated by higher formation rate of 2 nm particles (J_2) and the subsequent growth rate (GR)~~, even as NPF occurrence frequency slightly decreased~~. The relavent precursors, e.g. SO_2 and NO_2 showed a clear reduction, O_3 increased by 80% during LCD period, as compared with Pre_LCD. The volatile organic vapors showed different trends due to their sources. ~~The condensing vapors controlling the nucleation and growth process, sulfuric acid, and oxidation product of volatile organic compounds were estimated based on available information.~~ The proxy sulfuric acid~~values and organic oxidized vapors~~

25 ~~increased~~ during the LCD period increased by approximately ~~35~~26%, as compared with Pre_LCD~~, respectively~~. The major oxidants (O_3, OH and NO_3) of VOCs were also found to be elevated during LCD. That indicated ~~h~~Higher J_2 and GR (especially below 5 nm) during the LCD period were favored by the increased concentration level of condensing vapors and decreased condensation sink. Several heavy haze episodes have been reported by other studies during the LCD period; however, the increase in nanoparticle number concentration should also be considered. Some typical NPF events produced a high number

30 concentration of nanoparticles that intensified in the following days to create severe aerosol pollution. Our study confirms a significant enhancement of the nucleation and growth process of nanoparticles during the COVID-19 LCD in Beijing and highlights the necessity of controlling nanoparticles in current and future air quality management.

1. Introduction

As a response to the outbreak of the 2019 novel coronavirus (COVID-19), the Chinese government implemented restrictions on population movement in February 2020; the period when the restrictions were enforced was also called the lockdown period (LCD). During the LCD period, the NO_x emission was reduced by approximately 50% in China, as retrieved by the satellite (Zhang et al., 2021) and ground-based measurements (Huang et al., 2020). The number concentration of Aitken mode particles (~25-100 nm) should also decreased as expected, which is related with the traffic emission (Deventer et al., 2018) is also expected to decrease. The significant decrease in aerosol and precursor emissions during LCD is associated with reduced human and economic activities. However, several heavy haze pollution periods occurred in the Yangtze River Delta (YRD) and the Beijing–Tianjing–Hebei Province (BTH) region. Secondary particles contribute significantly to Air air pollution is driven by the enhancement of secondary particles, and NO_x reduction favors increased ozone and atmospheric oxidizing capacity (Huang et al., 2020). The aerosol heterogeneous reaction process was also enhanced by the anomalously high humidity in northern China (Le et al., 2020). Furthermore, particle accumulation was could also be favored by stagnant airflow and vertical meteorological conditions during LCD (Zhong et al., 2018) (Zhong et al., 2020).

New particle formation (NPF) has been an active global research topic for the last two decades because of its potential climatic implications (Kulmala et al., 2004). Nucleated particles can reach number concentrations of 10^4–10^6 cm^{-3}. Subsequent growth contributes significantly to cloud condensation nuclei (CCN) (Kerminen et al., 2012) and can cause air pollution (Guo et al., 2014). Primary emissions of particulate matter (PM), CO, SO_2, and NO_2 decreased significantly after the strict clear air action plans were implemented in the last decade by the Beijing government (Zhang et al., 2019). Changes in SO_2 and background aerosols, the key factors influencing NPF events, are also linked to the formation (J) and growth rates (GR) of secondary particles (Kyrö et al., 2014). Nanoparticles (diameter ≤ 100 nm) make minor particle mass contributions but pose a serious risk to human health because of high number concentrations and deep respiratory and cardiovascular system penetration (Kawanaka et al., 2009). However, the size-resolved, chemical, and toxicological properties of nanoparticles are unclear (Jin et al., 2017). Under unfavorable meteorological conditions, the growth of the nanoparticles for several consecutive days would even probably lead to particle mass enhancement as found in Beijing, China (Guo et al., 2014).

In a previous study, the influence of NPF event occurrence by emission reduction in Beijing was analyzed for China's Victory Day parade in August 2015 and for the summer Olympics in 2008; during this period, higher NPF occurrence frequency but lower J and GR was reported as a result of low precursor concentrations (Shen et al., 2016). In the present study, we focus on changes in particle number size distribution and NPF events during LCD in Beijing and the influencing factors. The link between NPF events and regional aerosol pollution is also explored. Our study will facilitate the optimization of regulatory measures to control particle and gas pollution in China, especially with regard to the variation of NPF-associated condensing

vapors caused by reduced precursor emissions and elevated atmospheric oxidizing level.

2.   Methods

2.1   Measurements

The particle and ion number size distribution measurements were conducted in January and February 2020 on the roof of the Chinese Academy of Meteorological Sciences building (CAMS) on the Chinese Meteorological Administration campus. The site is approximately 53 m above ground level and located in the western Beijing urban area between the second and third ring roads. A major road with heavy traffic to the west of the site indicated that the sample air could be influenced by traffic emissions. More information about the site can be found in X. Wang et al. (2018) Wang et al. (2018b)Wang et al. (2018b) Wang et al. (2018b).

2.2   Instrumentation

The number of particles of sizes 10–850 nm was measured using a scanning mobility particle sizer (SMPS, TROPOS, Germany). The system is a combination of a differential mobility analyzer (DMA) and a condensation particle counter (CPC, Model 3772, TSI Inc., USA). The mobility distribution of naturally charged and neutral nanoparticles is measured by a neutral cluster and air ion spectrometer (NAIS) with a 10-min time resolution (Mirme et al., 2007, Mirme and Mirme, 2013). The measured mobility was in the range 3.3–0.0013 $cm^2\,V^{-1}\,s^{-1}$, corresponding to mobility diameters of 0.8–42 nm. Positive and negative ions were simultaneously classified by two cylindrical differential mobility analyzers (DMAs) and detected with 21 electrometers on the outer cylinder. A high sample flow rate of 60 lpm was used to minimize diffusion losses. In ion mode, the detected signal is inverted to a mobility distribution consisting of 28 bins, taking into account the measured background and experimentally determined diffusion losses. In neutral particle mode, the sample aerosol is charged using corona chargers, and the charged fraction is calculated (Fuchs, 1963). However, the lowest detection limit for the NAIS in the neutral particle mode (approximately 2 nm) was affected by the corona-generated ions (Asmi et al., 2009, Manninen et al., 2011). The lowest detection limit of the NAIS in ion mode was determined by the charging probability, nanoparticle concentration, and charger ion mobility (Kulmala et al., 2013).

Volitale organic vapors (VOCs) were measured using a Proton Transfer Reaction-Time of Flight Mass Spectrometery (PTR-ToF-MS 8000, IONICON) with a hydronium ion (H_3O^+) source at CAMS site. About 30 kinds of compounds could be detected by the PTR-ToF-MS, by using the linear regression multipoint calibrations (Yuan et al., 2017). In this study, mixing ratio of isoprene and major C6–C9 VOCs were derived with 1 h time resolution, which are good indicators of anthropogenic VOC plumes (Dai et al., 2017).

The mass concentrations of PM$_{2.5}$, precursor gases of O$_3$, SO$_2$, NO$_2$, and CO at the GuanYuan air quality monitoring site were derived from the data center of the Ministry of Ecology and Environment of the People's Republic of China (http://datacenter.mep.gov.cn), which is 3 km from the CAMS site. The global radiation at the observatory (54511) in the southern Beijing urban area was used to estimate the sulfuric acid ~~and OH radials as proxies~~ in this work. The solar radiation

95 datasets were provided by the National Meteorological Information Center of the China Meteorological Administration. The meteorological factors used in this study—wind speed (WS), wind direction (WD), and relative humidity (RH)—were derived from the Haidian National Basic Meteorological Station (54399). The data can represent meteorological conditions at the CAMS site, which is located ~5 km northwest of the urban area site.

2.3 NPF parameter calculation

100 The total particle and ion formation rate at 2 nm ($J_{2,tot}$ and $J_{2,ion}$) can be calculated from the particle and ion number concentrations in the size range 2–3 nm (Hirsikko et al., 2011, Manninen et al., 2010). $J_{2,tot}$ and $J_{2,ion}$ included time changes in the concentration of 2–3 nm particles or ions (first term on the right side of Eq. 1 and 2), coagulation loss of 2–3 nm particles or ions with the pre-existing particles derived by SMPS (second term), and growth of 2–3 nm particles or ions into larger sizes by the growth rate, GR (third term). In Eq. (2), the fourth and fifth terms represent loss due to ion–ion recombination and

105 formation from ion-neutral attachment. The equations are given by the following formulas:

$$J_{2,tot} = \frac{dN_{2-3,tot}}{dt} + CoagS_2 \times N_{2-3,tot} + \frac{GR_3}{1nm} \times N_{2-3,tot} \qquad (1)$$

$$J_{2,ion}^{\pm} = \frac{dN_{2-3,ion}^{\pm}}{dt} + CoagS_2 \times N_{2-3,ion}^{\pm} + \frac{GR_3}{1nm} N_{2-3,ion}^{\pm} + \alpha \times N_{2-3,ion}^{\pm} N_{<3,ion}^{\mp}$$
$$- \beta \times N_{2-3,par} N_{<2,ion}^{\pm} \qquad (2)$$

$N_{2-3,tot}$ and $N^{\pm}_{2-3,ion}$ are the number concentration of particles and ions of positive and negative charges, respectively. $CoagS_2$ is

110 the 2 nm coagulation coefficient. α and β (the ion–ion recombination and ion-neutral attachment coefficients, respectively) are assumed to be 1.6×10^{-6} and 10^{-8} cm^{3}s^{-1}, respectively, (Hoppel, 1985).

Growth rate (GR) is defined as the rate of change of diameter with time, $GR = (D_{p,2} - D_{p,1})/dt$, given in nm h^{-1}, where $D_{p,1}$ and $D_{p,2}$ are the geometric mean diameters (GMD) when the nucleated particles start and stop growing, respectively. GMDs are derived by the log-normal modal fitting of the particle/ion number size distributions (Hussein et al., 2009).

115 Sulfuric acid (H$_2$SO$_4$) is a key component in the nucleation process (Kulmala et al., 2013). The concentration of H$_2$SO$_4$ was not measured directly in this study and different proxy methods were refered to derive the proxy sulfuric acid. A method (Eq. 3) ~~but can be estimated by~~ depends on the global radiation (Glob_R) ~~and~~, SO$_2$ and condensation sink (CS), and is developed according to the ~~chemical mass balance model recommended by~~ Petäjä et al. (2009) previous study conducted in a forest site, Hyytiälä, Finland (Petäjä et al., 2009). – Lu et al. (2019), Weber et al. (1997)~~:~~

4

120

$$[H_2SO_4] = \frac{k \times Glob\_R \times [SO_2]}{CS} \qquad (3)$$

where k is empirically derived factor and well correlated with Glob_R ($k=1.4\times10^{-7}\times$Glob_R$^{-0.7}$, unit: m^2 W^{-1} s^{-1}). The proxy equation is site-specific due to the different atmospheric comditions. In the polluted atmosphere, such as in Beijing, several proxy methods were also constructed based on a number of available atmospheric parameters (Lu et al., 2019). In this study, the simplext proxy (Eq. 4) and best performanced proxy (Eq. 5) in Lu et al. (2019) are adpotted to derive the proxy sulfuric

125   acid.

$$[H_2SO_4] = 280.05 \times UVB^{0.14} \times [SO_2]^{0.40} \qquad\quad \text{-} \quad (4)$$

$$[H_2SO_4] = 0.0013 \times UVB^{0.13} \times [SO_2]^{0.40} \times CS^{-0.17} \times ([O_3]^{0.44} + [NO_x]^{0.41}) \qquad (5)$$

where k is a constant scaling coefficient that depends on the location environment and is assumed to be 1 for simplicity in the estimation. [H$_2$SO$_4$] is the gaseous sulfuric acid with the unit of molecule cm^{-3}. [SO$_2$], [O$_3$] and [NO$_x$] is the concentration of

130   sulfur dioxide, ozone, and nitrogen oxides, with the unit of molecule cm^{-3}. UVB is the intensity of ultraviolet radiation b in W m^{-2}. CS is the condensation sink, which describes how fast the vapor molecules condense on the existing particles (Dal Maso et al., 2002), with the unit of s^{-1}. The proxy method has been validated by comparing the measured sulfuric acid with a high correlation coefficient of 0.86 (Lu et al., 2019), based on the field campaign conduted approximately 2 km away from CAMS site. Although the direct measurement of UVB was not available, it had been reported by Hu et al. (2013) that the monthly

135   average of the ratio of UVB to global radiation (Glob_R) ranged from 0.007 to 0.017% in Beijing. And in this study, the average ratio of January and Feburary (0.008%) was applied to to derive UVB by 0.008%$\times$ Glob_R. The covariance of CS and SO$_2$ was found (correlation coefficient R=0.83) that offset the dependence of sulfuric acid on CS by Lu et al. (2019). However, the anthropogenic emission sharply decreased during LCD in this study, and R was 0.45 between for SO$_2$ and CS. To minimize the uncertainty of H$_2$SO$_4$ proxy, the average value of three calculation methods was applied for the further analysis.

140   Highly oxidized biogenic organic vapors with extremely low volatility (ELVOCs) play an important role in the growth process of nucleated particles (Kulmala et al., 2014). As ELVOCs and their precursors were not available in this work, we used a surrogate method to formulate the concentration of the oxidized VOC products as follows (Kontkanen et al., 2016):

$$[VOC_{ox}] = \frac{k_{VOC,OH}[OH][VOC] + k_{VOC,O_3}[O_3][VOC]}{CS} \qquad (46)$$

where [VOC], [O_3], and [OH] are the precursor concentrations, $k_{VOC,OH}$ and k_{VOC,O_3} are the chemical rate coefficients in the

145   daytime VOC reactions with the dominant atmospheric oxidants OH and O$_3$, respectively (Atkinson et al., 2006). This method was used and validated in urban Beijing to study the contribution of VOC oxidation products to the growth of nucleated particles (Wang et al., 2015). VOC was not measured in this study; thus, we only considered the oxidizingation capacity variation during measurement, which was denoted as follows:

$$[VOC_{ox,capacity}] = \frac{k_{VOC,OH}[OH] + k_{VOC,O_3}[O_3]}{CS} \qquad (57)$$

The concentration of OH was calculated by scaling the measured ultraviolet radiation B (UVB) radiation using the following recommended empirical equation (Nieminen et al., 2014) (Petäjä et al., 2009):

$$[OH]_{proxy} = (\frac{8.4 \times 10^{-7}}{8.6 \times 10^{-10}} UVB^{0.32})^{1.92} \qquad (68)$$

As with sulfuric acid estimation, global radiation (Glob_R) was applied because of the lack of UVB measurement. The concentrations of condensing vapors are estimated roughly in this work due to the lack of direct measurements of some key parameters, and thus can not represent the real level in the atmosphere, but reflect the variation trends of each parameter on NPF days during different periods.

2.4 Typical NPF event identification

NPF events are identified and different nucleation types are characterized based on the daily evolution of particle number size distribution (PNSD). The burst of nucleation mode particles with diameter ≤ 25 nm appeared in the PNSD, and the burst should prevail over a few hours with clear growth process (Dal Maso et al., 2005). Regional NPF events can occur over a geographically large area and extend over several hundreds of kilometers (Shen et al., 2018). Such events indicate regional cases in which freshly nucleated particles can reach the size of CCN (Shen et al., 2011).

2.5 Back trajectory analysis

In order to reveal the meteorological condition during the pollution case formation, the 48 h backward trajectories arriving at CAMS stie were calculated at 12:00 Local time during February 4-14 for case study, terminating at the height of 500 m above ground level by applying the Trajstat Software, combined with HYSPLIT 4 model (Hybrid Single-Particle Lagrangian Integrated Trajectory) and using the NCEP GDAS (Global Data Assimilation System) data with 1°×1° resolution (Draxler and Hess, 1998, Wang et al., 2009).

3. Results and discussion

3.1 The meteorological conditions

The meteorological parameters during LCD period, January and February in 2020, as well as the average conditions of January and February in 2016-2020 were analyzed and the diurnal pattern was given (Fig. 1). It showed much higher RH, lower WS, slightly higher T and lower pressure during LCD, January and February 2020, than that of 5-year climatology average condition (January and February in 2016-2020). The anomaly of monthly mean sea level pressure in January and February between 2020 and 2016-2020 was analyzed based on the ECMWF reanalysis dataset (ERA5,

3.13.2   Overview of the NSD of particles and charged ions

Fig. 12 shows the time evolution of the number size distribution (NSD) of particles in the 10–850 nm range, neutral particles (2–42 nm), and charged ions (0.8–42 nm) in January and February 2020. The dataset was classified into the COVID-19 LCD (January 24–February 16, 2020), prePre-LCD period (January 3–23, 2020), and postPost-LCD (February 17–29, 2020) to

185   reveal the influence of emission reductions. The NPF event occurred on 10 out of 23 days (43%) during prePre-LCD, 810 out of 24 days (33%) in LCD, and 5 out of 13 days (38%) in postPost-LCD, respectively. Poisson statistics was conducted for NPF event occurrence probability for Pre LCD, LCD and Post LCD period, respectively, as given in Fig. S2 in supplementary materials. It showed slight variation of NPF event occurrence probability, as compared with Pre LCD and LCD period. NPF occurrence frequency was slightly lower during LCD. Despite large primary emissions reduction, several cases

190   of heavy aerosol pollution events occurred in the BTH region during LCD. Particle matter below 2.5 μm ($PM_{2.5}$) mass concentration at air monitoring sites in Beijing of the Ministry of Ecology and Environment of China exceeded 75 μg/m^3 (the second grade of the Ambient Air Quality Standard of China) on 12 of the 28 days, which were identified as polluted conditons. The elevated PM mass concentration was attributed to the secondary aerosol formation process; this process was aided by the enhanced oxidizing capacity caused by increased ozone levels (Huang et al., 2020). The meteorological analysis also revealed

195   that an inversion layer occurred in the BTH region and trapped moisture and pollutants near the ground, thus offsetting substantial emissions reductions during COVID-19 LCD (Zhong et al., 2018) (Zhong et al., 2020).

The particle number concentrations of the Aitken mode (25–100 nm, $N_{25-100nm}$) and the accumulation mode (100–850 nm, $N_{100-850nm}$) derived by SMPS and the nucleation mode (≤ 25 nm) of neutral particles and charged ions by NAIS were discussed in detailwere given in Fig. 2a3 and discussed in detail in the following. The Aitken mode showed a significant reduction since

200   the Chinese New Year (January 24) and normal fluctuations below 3000 cm^{-3} during LCD and postPost-LCD. Mean N_{25-100} concentrations were 4040 ± 1590, 2400 ± 1170, and 2170 ± 994 cm^{-3} in prePre-LCD, LCD, and postPost-LCD, respectively. Aitken mode particles were closely related to the anthropogenic emissions and reduced by approximately 40%. During postPost-LCD, the Aitken mode concentration remained low because people were encouraged to work at home and services were almost shut down. Accumulation mode particles usually undergo coagulation, condensation, heterogeneous reactions,

205   and long-range transport processes that can reflect regional polluted conditions. $N_{100-850nm}$ concentrations were 1820 ± 1190,

2200 ± 1320, and 1850 ± 840 cm^{-3} during ~~pre~~Pre -LCD, LCD, and ~~post~~Post- _LCD, respectively; the 20% increase during LCD (compared with ~~pre~~Pre_ -LCD) occurred despite large emissions reductions and was related to specific pollution episodes that occurred from January 24–26 and February 12–14. The particle number concentration derived from SMPS is probably lower than that from NAIS in the overlap size range of 20–40 nm, because the overestimation of natural particle concentration as a multiple charge effect above 20 nm is beyond the instrumental detection limit (Gagné et al., 2011). In this study, the number concentration of 20–40 nm was integrated by the SMPS and NAIS particle mode ($N_{20–40nm, smps}$ and $N_{20–40nm, nais}$) with an enhancement factor ($N_{20–40nm, nais}/N_{20–40nm, smps}$) of 1.65 ± 0.06, and the number concentration of particles larger than 20 nm derived by SMPS was more accurate.

The nucleation mode ($N_{par, \leq 25\ nm}$) derived from NAIS was separated into ≤ 10 nm and 10–25 nm for neutral particles ($N_{par,nais,2–10nm}$, $N_{par,nais,10–25nm}$) and positively charged ions ($N_{ion,nais,1–10nm}$, $N_{ion,nais,10–25nm}$), respectively. $N_{par,nais,2–10nm}$ was the primary contributor to the nucleation mode, which was determined by NPF events, during which average peak $N_{par,nais,\leq 25\ nm}$ concentrations were $2.3 \pm 2.3 \times 10^4$, $1.5 \pm 2.6 \times 10^4$, and $1.9 \pm 3.3 \times 10^4$ cm^{-3}, during ~~pre~~Pre- _LCD, LCD, and ~~post~~Post- _LCD, respectively (Fig. ~~2b~~3b). The number concentration of 10–25 nm particles could also be derived from SMPS ($N_{par,smps,10-25nm}$), which was also given in Fig. ~~2b~~ 3b and approximately 30% lower than the value of $N_{par,nais,10-25nm}$. $N_{par, \leq 25\ nm}$ showed large variation because of significant differences between NPF and non-NPF days. However, several cases during LCD showed a significantly high peak $N_{par,2–10nm}$ value (Fig. ~~2~~3c), indicating the probability of the stronger nucleation process during LCD. The positive and negative ion number concentrations of 0.8–42 nm were 457 ± 245 and 496 ± 265 cm^{-3}, respectively. The mean values of $N_{ion,nais,1–10nm}$ and $N_{ion,nais,10–25nm}$ ranged from 100–200 cm^{-3}, indicating a minor contribution to the total particle count.

~~3.2~~3.3   NPF event variation

Table 1 provides the key parameters describing NPF events, including NPF ~~frequency~~days and available measurement days, CS, J_2, and GR for total particles and charged ions. Higher J_2 and GR values for particles and ions were also found during LCD and ~~post~~Post -LCD than during ~~pre~~Pre- _LCD. However, the emissions control period during the China Victory Parade in Beijing in 2015 (August 20–September 3) featured higher frequency, decreasing J_3 and GR trends compared with the corresponding month in 2010–2013 (Shen et al., 2016). J_3 referred the formation rate at 3 nm calculated from the particle number concentration of 3–4 nm particles by Eq. (1), as the lowest detection limit of SMPS applied in 2015 and 2010-2013 campaign was 3 nm. That indicated the factors influencing the NPF event, including precursors, pre-existing particles and meteorological conditions, were complex and should be evaluated further. ~~In this study, t~~The daily mean value of NO$_2$ decreased by ~35% and SO$_2$ decreased by ~13%, whereas O$_3$ increased by 80% during LCD as compared to ~~pre~~Pre- _LCD in this work (Fig. ~~3~~4). The probability density function (PDF) was analyzed for hourly SO$_2$, NO$_2$ and O$_3$ during Pre_LCD, LCD

and Post_LCD, respectively and the result was given in the supplementary materials (Fig. S3). It also showed significant decreasing trend of NO_2, whereas increasing trend of O_3 as compared with Pre_LCD and LCD/Post_LCD. However, the variation of SO_2 among different periods was not clear, as the SO_2 concentration remained low due to the emission control these years. ~~The p~~Previous stud~~ies had y~~indicated that NO_x ~~suppresses~~ suppressed NPF events by influencing the formation of highly oxygenated organic molecules (HOMs), which participated in nucleation and initial particle growth (Lehtipalo et al., 2018, Yan et al., 2016, 2020) ~~(Lehtipalo et al., 2018, Yan et al., 2016, Yan et al., 2020)~~, suggesting ~~(Zhang et al., 2021)~~ that the reduction of NO_2 during LCD provided favorable conditions for particle growth.

In this work, five kinds of VOCs (isoprene, benzene, toluene, C8 and C9 aromatics) are discussed, which are the indicators of anthropogenic VOC and also could be oxidized to be HOMs to contribute to the growth process (Dai et al., 2017). The result (Fig. 5) showed C8 and C9 aromatics decreased by approximately 20% and 8% during LCD as compared with Pre_LCD, however, isoprene and toluene slightly changed, benzene increased by approximately 21% during LCD period. It also suggested the VOCs we focused didn't show the reduction rate as 45% as Huang et al. (2020) reported in BTH region. The major pathways of HOMs formation are the oxidation by O_3, OH and NO_3 radicals (Atkinson and Arey, 2003). As mentioned above, O_3 increased by 80% during LCD period. We used Glob_R as a simple proxy of OH, and Glob_R increased by ~24% during LCD as compared with Pre_LCD, as given in the supplementary materials (Fig. S4). NO_3 oxidation of nocturnal biogenic VOCs is also an important pathway of secondary organic aerosol formation in Beijing (H. Wang et al., 2018) ~~(Wang et al., 2018)~~. NO_3 is predominantly formed by the reaction of NO_2 with O_3 ($NO_2 + O_3 \rightarrow NO_3 + O_2$), and we applied $[NO_2] \times [O_3]$ to estimate the NO_3 production. It showed $[NO_2] \times [O_3]$ term increased by ~40% during LCD period. ~~In general~~Based on the above discussion, it showed the variations of precursors, solar radiation and *CS* could finally influence NPF by photochemical reactions with VOCs and sulfuric acid production, promoting the nucleation and growth process ~~as discussed in the following section~~.

The H_2SO_4 ~~and low volatility organic vapor~~ proxy were derived according to equations (3–~~6~~5) as given in Fig. 6 and the mean value of the three mothds was discussed~~; Fig. 4 presents the estimated values~~. ~~As discussed separately f~~For LCD and ~~pre~~Pre_LCD during the NPF event occurrence (9:00–16:00 LT), *CS* decreased by ~25% and Glob_R increased by ~40%, whereas SO_2 decreased by ~28%. The variations of these variables finally lead to a H_2SO_4 increase of ~~35~~26%. The formation of sulfuric acid was aided by the enhanced atmospheric oxidizing capacity because of elevated O_3 concentration during LCD, which had also been validated in the previous study in Nanjing, YRD, China (Huang et al., 2020). ~~It also reported that VOC emissions in the BTH region were reduced by ~45% (Huang et al., 2020), but oxidized capacity was enhanced by ~50% based on our estimation during LCD period. Especially on NPF days, the VOC oxidizing~~ation ~~capacity enhancement factor was ~1.3. Thus, the oxidization~~ oxidizing ~~product with low volatility probably increased and offset the reduction of VOC emissions, and~~

favored particle growth. ~~These results are consistent with those of a previous study showing that elevated O₃ promoted SO₂ oxidation into sulfate and VOCs into low volatility vapors, which condensed onto the particle surface and contributed to the nucleation and growth process (Ehn et al., 2014).~~

~~Both The correlation between t~~The H₂SO₄ proxy ~~and the VOC~~$_{ox,capacity}$~~were correlated to~~with $J_{2,tot}$ ~~(GR)~~and to GR~~,~~ respectively. ~~, was indicated by different VOC$_{ox,capacity}$ levels as shown in Fig. 5. GR showed higher values corresponding to high concentrations of condensing vapors.with t~~The ~~correlation coefficient (R value) was~~of 0.~~56~~62 for $J_{2,tot}$ and the H₂SO₄, and 0.~~62~~45 for GR and the H₂SO₄, respectively. Based on the NAIS data of neutral particle mode, the hourly mean geometric mean diameter of nucleation mode ($D_{p,nuc}$) was fitted to show the growth process and ~~the~~its relationship with proxy H₂SO₄ ~~was dicussed~~(Fig. 7). It also revealed that in the initial growth process ($D_{p,nuc}$< 5 nm), $D_{p,nuc}$ increased positively with H₂SO₄ proxy. Furthermore, GR in the size range of 3-5 nm was slightly higher during LCD and Post_LCD, as compared with Pre_LCD, indicating the enhanced effect of sulfuric acid on the initial growth of the nucleated particles. However, when the nucleated particles grew into the larger sizes (> 5 nm), H₂SO₄ proxy decreased probably related with the weak solar radiation in late afternoon, which could not explain the continuous growth and the oxidized VOCs could be the main contributor. ~~R was 0.74 and 0.60, respectively, for the correlation between J$_{2,tot}$ and VOC$_{ox,capacity}$ and GR and VOC$_{ox,capacity}$, respectively.~~ The non-linear dependence of $J_{2,tot}$, and GR on the condensing vapors indicates a complex mechanism in the multi-component nucleation and growth system. Stolzenburg et al. (2020) ~~showed~~revealed that ~~When the particles overcame the criteria size of 10 nm,~~ sulfuric acid ~~which plays~~played an important role in smaller growth processes from 2–10 nm~~—~~, however, could not explain condensational growth when the nucleated particles overcame 10 nm ~~(Stolzenburg et al., 2020)~~. For particles larger than 10 nm, low volatile organic vapors should contribute to growth (Kontkanen et al., 2018, Yan et al., 2020). ~~The general increase in J₂ and GR during LCD compared with pre LCD was probably related to the increase in the sulfuric acid concentration and VOC oxidization oxidizing capacity.~~

~~3.3~~3.4   Effect of charged ions

Table 1 ~~provides~~provided the parameters describing the nucleation and growth process for neutral particles and positive and negative ions and ~~shows~~showed that the GR of ions was larger than that of neutral particles. Growth enhancement from charge–dipole interactions between condensable gases and charged ions lead to higher growth rates than with neutral particles (Nadykto and Yu, 2003, Yu and Turco, 2000). The growth process of $D_{p,nuc}$ of neutral particles and positive ions were given in Fig. 8. It showed $D_{p,nuc,ion}$ grow faster than $D_{p,nuc,par}$, especially for the sizes below 5 nm, depending on the growth rate in each time interval (($D_{p,nuc,t1}$- $D_{p,nuc,t2}$)/Δt, Δt = 1 h). The enhanced growth rate factor ($GR_{p,nuc,ion}$/ $GR_{p,nuc,par}$) ranged from 1.1 to 1.7, with the average of 1.38±0.34 during the entire particle growth process and higher (~2.0) for the initial size of 2–5 nm. The growth of the nano-sized particles was not linear (especially at the initial size); therefore, the GR calculation was split into

different size ranges (Fig. 6̶9). The *GR* of charged ions was higher than that of neutral particles for all size ranges, which is consistent with previous studies (Hirsikko et al., 2005, Suni et al., 2008), and the difference was much larger at initial sizes below 5 nm as indicated above. In addition to condensational growth, the difference in the loss rates of smaller particles (neutral, positive, negative) due to the coagulation process and ion–ion recombination also affects particle size and calculated *GRs* (Yu and Turco, 2008, 2011). ~~Growth enhancement from charge-dipole interactions between condensable gases and charged ions lead to higher growth rates than with neutral particles (Nadykto and Yu, 2003, Yu and Turco, 2000). The enhancement factor due to the charge effect was 1.35 ± 0.35 during the entire particle growth process and higher (~2.0) for the initial size of 2–5 nm. These results were comparable with the experimental laboratory demonstration of an enhancement factor of 1.8–3.2 nm due to the charge effect (Stolzenburg et al., 2020).~~ The effect of the charge̶r decreases as particle size increases, and more species condense as particles grow. However, the number concentration of charged ions plays a minor role in the total particle count, and their contribution to the total growth process and nucleation can be ignored in urban Beijing, where the nucleation mechanism is dominated by neutral pathway with abundant condensing vapors.

3.4̶3.5   Air pollution episode followed by NPF event

In this study, t̶Two severe pollution episodes occurred during LCD from January 24–29 and February 7–14, with daily average PM$_{2.5}$ mass concentrations in the range 75–210 μg/m^3. Both episodes occurred after NPF days on January 23 (No. 10) and February 4 (No. 1̶516), respectively. Other pollution episodes in January 16–18, February 19–21, and February 28–29 were preceded by NPF events No. 8, 21, and 25, respectively. The most long-lasting pollution episode on February 7–14 is discussed further to reveal the relationship between NPF events and aerosol pollution formation (Fig. 7̶10). The NPF events on February 4–5 produced high concentrations of nucleation mode particles, which grew to 150–200 nm in a few days. Two principal pollution episode formation stages were identified according to variations in the PM$_{2.5}$ mass concentration dividing by CO (PM$_{2.5}$/CO), as indicated in Fig. 7̶10b. The normalized PM$_{2.5}$ by CO represents the secondary aerosol formation effect, which segregates the possible influence of physical effects, such as air mass change and planetary boundary layer (PBL) development (Wiedensohler et al., 2009). The back trajectories arriving at CAMS station at 12:00 local time form February 4 to 14 with the terminal height of 500 m agl were calculated (Fig. 8̶11). The result showed back trajectories originated from northwest from February 4 to 10, corresponding to the dry and clean air masses. However, from February 11 to 13, the southwesterly air masses were dominated and favored the accumulating of the particles, resulting in the high concentration level of PM$_{2.5}$. In the first stage (February 5–1̶110), the secondary aerosol formation was the key process contributing to increasing PM$_{2.5}$ mass. The continuous growth of nucleated particles was intervened by the development of PBL and local wind sometimes. As in the second stage (February 11–13), PM$_{2.5}$ reached a peak value of 250 μg/m^3, and PM$_{2.5}$/CO slightly decreased with small fluctuations. Because primary emission should not change during this period, ~~and~~ the unfavorable

meteorological conditions could be responsible for the event. ~~During this period, northeasterly and southwesterly winds were dominant, whereas the WS was normally lower than 2 m/s.~~ Low WS and high RH ~~remained high~~ (from 80% to >90%) was found from February 5–14, with a few hours of RH <60% during the daytime. Particle hygroscopic growth under high ambient RH conditions and heterogeneous reactions on particle surfaces could also contribute to the elevated particle mass concentration (X. Wang et al., 2018) ~~(Wang et al., 2018b)~~. Consequently, nucleated particles accumulated because of enhanced oxidizing capacity and favorable meteorological conditions and caused severe aerosol pollution.

4. Conclusion

In this study, we presented changes in the NSD of particles and charged ions measured in January and February 2020 to reveal the influence of emission reduction on NPF events. Particles smaller than 100 nm were effectively reduced by ~40% because of suspended human activities during the Chinese New Year and the COVID-19 LCD. The accumulation mode particles were slightly higher during LCD, as several hazy days were associated with secondary aerosol formation. The frequency of NPF days ~~was~~ slightly ~~lower during LCD as compared with pre-LCD period~~varied; however, J_2 and GR were significantly higher. ~~Enhanced formation and growth rates were related to the elevated oxidation capacity of the atmosphere, which could be seen from the increase of sulfuric acid concentration proxy and VOC oxidization oxidizing capacity.~~ During LCD, NO_x and SO_2 concentrations decreased as anthropogenic emissions were reduced. Higher O_3 and a lower condensation sink raised sulfuric acid concentration levels by ~~35~~26% ~~and VOC oxidization oxidizing capacity by a factor of 1.3 on NPF days~~, which were responsible for the higher nucleation rate and larger nanoparticle quantity. Sulfuric acid was also responsible for the nucleated particle growth at the initial sizes (below 5 nm). In the late afternoon, sulfuric acid decreased as the weakend solar radiation and low volatility oxidation products of VOCs could have larger contribution to the particle growth. ~~For the~~ major VOCs, isoprene and toluene were slightly changed, benzene increased, and aromatics (C8 and C9 componds) decreased during LCD period. Although the oxidation products of VOCs were not measured in this study, the major oxidants of VOCs (O_3, OH and NO_3) all increased during LCD period, indicating the possibility of enhanced HOMs promoting the particle growth process. The effect of charge ions on the particle growth was also studies and it showed a enhanced growth rate facotor of 1.38±0.34. ~~The elevated sulfuric acid concentration and VOC oxidization oxidizing capacity could explain the higher $J_{2,tot}$ and GR to some extent.~~ The nucleated particles entered accumulation mode by the secondary aerosol formation and underwent hygroscopic growth under high RH and calm wind conditions, which facilitated the occurrence of severe pollution episodes during LCD. This work highlights the potential influence of strict emission control strategies on NPF events and provides insights into the positive and negative effects of precursors and atmospheric oxidizing capacity on the nucleation and growth process of the nanoparticles.

References

Asmi, A., Sipilä, M., Manninen, H. E., Vanhanen, J., Lehtipalo, K., Gagné, S., Neitola, K., Mirme, A., Mirme, S., E, T., Uin, J., Komsaare, K., Attoui, M. and Kulmala, M.: Results of the first air ion spectrometer calibration and intercomparison workshop, Atmos. Chem. Phys., 9: 141-154, 2009.

Atkinson, R. and Arey, J.: Gas-phase tropospheric chemistry of biogenic volatile organic compounds: a review, Atmospheric Environment, 37: 197-219, DOI: 10.1016/s1352-2310(03)00391-1, 2003.

Dai, L., Wang, H., Zhou, L., An, J., Tang, L., Lu, C., Yan, W., Liu, R., Kong, S., Chen, M., Lee, S. and Yu, H.: Regional and local new particle formation events observed in the Yangtze River Delta region, China, J. Geophys. Res., 122(4): 2389-2402, DOI: 10.1002/2016jd026030, 2017.

Dal Maso, M., Kulmala, M., Lehtinen, K. E. J., Mäkelä, J. M., Aalto, P. and O'Dowd, C. D.: Condensation and coagulation sinks and formation of nucleation mode particles in coastal and boreal forest boundary layers, J. Geophys. Res., 107(D19): 10.1029/2001JD001053, 2002.

Dal Maso, M., Kulmala, M., Riipinen, I., Wagner, R., Hussein, T., Aalto, P. P. and Lehtinen, K. E. J.: Formation and growth of fresh atmospheric aerosols: eight years of aerosol size distribution data from SMEAR II, Boreal Environ. Res., 10: 323–336, 2005.

Deventer, M. J., von der Heyden, L., Lamprecht, C., Graus, M., Karl, T. and Held, A.: Aerosol particles during the Innsbruck Air Quality Study (INNAQS): Fluxes of nucleation to accumulation mode particles in relation to selective urban tracers, Atmos. Environ., 190: 376-388, DOI: 10.1016/j.atmosenv.2018.04.043, 2018.

Draxler, R. R. and Hess, G. D.: An overview of the HYSPLIT_4 modelling system of trajectories, dispersion, and deposition, Aust. Meteor. Mag.,, 47: 295-308, 1998.

Fuchs, N. A.: On the stationary charge distribution on aerosol particles in bipolar ionic atmosphere, Geofis. Pura Appl., 56: 185-193, 1963.

Gagné, S., Lehtipalo, K., Manninen, H. E., Nieminen, T., Schobesberger, S., Franchin, A., Yli-Juuti, T., Boulon, J., Sonntag, A., Mirme, S., Mirme, A., Hõrrak, U., Petäjä, T., Asmi, E. and Kulmala, M.: Intercomparison of air ion spectrometers: an evaluation of results in varying conditions, Atmos. Meas. Tech., 4(5): 805-822, DOI: 10.5194/amt-4-805-2011, 2011.

Guo, S., Hu, M., Zamora, M. L., Peng, J., Shang, D., Zheng, J., Du, Z., Wu, Z., Shao, M., Zeng, L., Molina, M. J. and Zhang, R.: Elucidating severe urban haze formation in China, Proc Natl Acad Sci, 111(49): 17373-17378, DOI: 10.1073/pnas.1419604111, 2014.

Hirsikko, A., Laakso, L., Aalto, P. P., Kerminen, V.-M., Hõrrak, U. and Kulmala, M.: Annual and size dependent variation of growth rates and ion concentrations in boreal forest, Boreal Envrion. Res., 10: 357–369, 2005.

Hirsikko, A., Nieminen, T., Gagné, S., Lehtipalo, K., Manninen, H. E., Ehn, M., Hõrrak, U., Kerminen, V. M., Laakso, L., McMurry, P. H., Mirme, A., Mirme, S., Petäjä, T., Tammet, H., Vakkari, V., Vana, M. and Kulmala, M.: Atmospheric ions and nucleation: a review of observations, Atmos. Chem. Phys., 11(2): 767-798, DOI: 10.5194/acp-11-767-2011, 2011.

Hoppel, W. A.: Ion-Aerosol Attachement Coefficients, Ion Depletion, and the Charge Distribution on Aerosols, J. Geophys. Res., 90: 5917–5923, 1985.

Hu, B., Zhang, X. H. and Wang, Y. S.: Variability in UVB radiation in Beijing, China, Photochem Photobiol, 89(3): 745-750, DOI: 10.1111/php.12051, 2013.

Huang, X., Ding, A., Gao, J., B. Zheng, D. Zhou, X. Qi, R. Tang, J. Wang, C. Ren, W. Nie, X. Chi, Z. Xu, L. Chen, Y. Li, F. Che, N. Pang, H. Wang, D. Tong, W. Qin, W. Cheng, W. Liu, Q. Fu, B. Liu, F. Chai, S.J. Davis, Q. Zhang and K. He. Enhanced secondary pollution offset reduction of primary emissions during COVID-19 lockdown in China, National Sci Rev, nwaa137, 2020.

Hussein, T., Junninen, H., Tunved, P., Kristensson, A., Maso, M. D., Riipinen, I., Aalto, P. P., Hansson, H.-C., Swietlicki, E. and Kulmala, M.: Time span and spatial scale of regional new particle formation events over Finland and Southern Sweden, Atmos. Chem. Phys., 9: 4699–4716, 2009.

Jin, L., Luo, X., Fu, P. and Li, X.: Airborne particulate matter pollution in urban China: a chemical mixture perspective from sources to impacts, National Sci Rev, 4(4): 593-610, DOI: 10.1093/nsr/nww079, 2017.

Kawanaka, Y., Tsuchiya, Y., Yun, S. J. and Sakamoto, K.: Size distributions of polycyclic aromatic hydrocarbons in the atmosphere and estimation of the contribution of ultrafine particles to their lung deposition, Environ Sci Technol, 43: 6851–6856, 2009.

Kerminen, V. M., Paramonov, M., Anttila, T., Riipinen, I., Fountoukis, C., Korhonen, H., Asmi, E., Laakso, L., Lihavainen, H.,

Swietlicki, E., Svenningsson, B., Asmi, A., Pandis, S. N., Kulmala, M. and Petäjä, T.: Cloud condensation nuclei production associated with atmospheric nucleation: a synthesis based on existing literature and new results, Atmos. Chem. Phys., 12(24): 12037-12059, DOI: 10.5194/acp-12-12037-2012, 2012.

Kontkanen, J., Olenius, T., Kulmala, M. and Riipinen, I.: Exploring the potential of nano-Köhler theory to describe the growth of atmospheric molecular clusters by organic vapors using cluster kinetics simulations, Atmos. Chem. Phys., 18(18): 13733-13754, DOI: 10.5194/acp-18-13733-2018, 2018.

Kulmala, M., Kontkanen, J., Junninen, H., Lehtipalo, K., Manninen, H. E., Nieminen, T., Petaja, T., Sipila, M., Schobesberger, S., Rantala, P., Franchin, A., Jokinen, T., Jarvinen, E., Aijala, M., Kangasluoma, J., Hakala, J., Aalto, P. P., Paasonen, P., Mikkila, J., Vanhanen, J., Aalto, J., Hakola, H., Makkonen, U., Ruuskanen, T., Mauldin, R. L., Duplissy, J., Vehkamaki, H., Back, J., Kortelainen, A., Riipinen, I., Kurten, T., Johnston, M. V., Smith, J. N., Ehn, M., Mentel, T. F., Lehtinen, K. E. J., Laaksonen, A., Kerminen, V. M. and Worsnop, D. R.: Direct Observations of Atmospheric Aerosol Nucleation, Science, 339(6122): 943-946, DOI: 10.1126/science.1227385, 2013.

Kulmala, M., Vehkamäki, H., Petäjä, T., Dal Maso, M., Lauri, A., Kerminen, V. M., Birmili, W. and McMurry, P. H.: Formation and growth rates of ultrafine atmospheric particles: a review of observations, J. Aerosol Sci., 35(2): 143-176, DOI: 10.1016/j.jaerosci.2003.10.003, 2004.

Kyrö, E. M., Väänänen, R., Kerminen, V. M., Virkkula, A., Petäjä, T., Asmi, A., Dal Maso, M., Nieminen, T., Juhola, S., Shcherbinin, A., Riipinen, I., Lehtipalo, K., Keronen, P., Aalto, P. P., Hari, P. and Kulmala, M.: Trends in new particle formation in eastern Lapland, Finland: effect of decreasing sulfur emissions from Kola Peninsula, Atmos. Chem. Phys., 14(9): 4383-4396, DOI: 10.5194/acp-14-4383-2014, 2014.

Le, T., Wang, Y., Liu, L., Yang, J., Yung, Y. L., Li, G. and Seinfeld, J. H.: Unexpected air pollution with marked emission reductions during the COVID-19 outbreak in China, Science, 10.1126/science.abb7431, 2020.

Lehtipalo, K., Yan, C., Dada, L., Bianchi, F., Xiao, M., Wagner, R., Stolzenburg, D., Ahonen, L. R., Amorim, A., Baccarini, A., Bauer, P. S., Baumgartner, B. and Bergen, A.: Multicomponent new particle formation from sulfuric acid, ammonia, and biogenic vapors, Science Advance, 4: eaau5363, 2018.

Lu, Y., Yan, C., Fu, Y., Chen, Y., Liu, Y., Yang, G., Wang, Y., Bianchi, F., Chu, B., Zhou, Y., Yin, R., Baalbaki, R., Garmash, O., Deng, C., Wang, W., Liu, Y., Petäjä, T., Kerminen, V. M., Jiang, J., Kulmala, M. and Wang, L.: A proxy for atmospheric daytime gaseous sulfuric acid concentration in urban Beijing, Atmos. Chem. Phys., 19(3): 1971-1983, DOI: 10.5194/acp-19-1971-2019, 2019.

Manninen, H. E., Franchin, A., Schobesberger, S., Hirsikko, A., Hakala, J., Skromulis, A., Kangasluoma, J., Ehn, M., Junninen, H., Mirme, A., Mirme, S., Sipilä, M., Petäjä, T., Worsnop, D. R. and Kulmala, M.: Characterisation of corona-generated ions

used in a Neutral cluster and Air Ion Spectrometer (NAIS), Atmos. Meas. Tech., 4(12): 2767-2776, DOI: 10.5194/amt-4-2767-2011, 2011.

Manninen, H. E., Nieminen, T., Asmi, E., Gagné, S., Häkkinen, S., Lehtipalo, K., Aalto, P., Vana, M., Mirme, A., Mirme, S., Hõrrak, U., Plass-Dülmer, C., Stange, G., Kiss, G., Hoffer, A., Törő, N., Moerman, M., Henzing, B., de Leeuw, G., Brinkenberg, M., Kouvarakis, G. N., Bougiatioti, A., Mihalopoulos, N., O'Dowd, C., Ceburnis, D., Arneth, A., Svenningsson, B., Swietlicki, E., Tarozzi, L., Decesari, S., Facchini, M. C., Birmili, W., Sonntag, A., Wiedensohler, A., Boulon, J., Sellegri, K., Laj, P., Gysel, M., Bukowiecki, N., Weingartner, E., Wehrle, G., Laaksonen, A., Hamed, A., Joutsensaari, J., Petäjä, T., Kerminen, V. M. and Kulmala, M.: EUCAARI ion spectrometer measurements at 12 European sites – analysis of new particle formation events, Atmos. Chem. Phys., 10(16): 7907-7927, DOI: 10.5194/acp-10-7907-2010, 2010.

Mirme, A., Tamm, E., Mordas, G., Vana, M., Uin, J., Mirme, S., Bernotas, T., Laakso, L., Hirsikko, A. and Kulmala, M.: A wide- range multi-channel Air Ion Spectrometer, Boreal Environ. Res., 12: 247–264, 2007.

Mirme, S. and Mirme, A.: The mathematical principles and design of the NAIS – a spectrometer for the measurement of cluster ion and nanometer aerosol size distributions, Atmos. Meas. Tech., 6(4): 1061-1071, DOI: 10.5194/amt-6-1061-2013, 2013.

Nadykto, A. B. and Yu, F.: Uptake of neutral polar vapor molecules by charged clusters/particles: Enhancement due to dipole-charge interaction, J. Geophys. Res., 108(D23), DOI: 10.1029/2003jd003664, 2003.

Petäjä, T., Mauldin, I. R. L., Kosciuch, E., McGrath, J., Nieminen, T., Paasonen, P., Boy, M., Adamov, A., Kotiaho, T. and Kulmala, M.: Sulfuric acid and OH concentrations in a boreal forest site, Atmos. Chem. Phys., 9(19): 7435-7448, DOI: 10.5194/acp-9-7435-2009, 2009.

Riipinen, I., Yli-Juuti, T., Pierce, J. R., Petäjä, T., Worsnop, D. R., Kulmala, M. and Donahue, N. M.: The contribution of organics to atmospheric nanoparticle growth, Nature Geoscience, 5(7): 453-458, DOI: 10.1038/ngeo1499, 2012.

Shen, X. J., Sun, J., Kivekäs, N., Kristensson, A., Zhang, X., Zhang, Y., Zhang, L., Fan, R., Qi, X., Ma, Q. and Zhou, H.: Spatial distribution and occurrence probability of regional new particle formation events in eastern China, Atmos. Chem. Phys., 18(2): 587-599, DOI: 10.5194/acp-18-587-2018, 2018.

Shen, X. J., Sun, J. Y., Zhang, X. Y., Zhang, Y. M., Zhang, L., Fan, R. X., Zhang, Z. X., Zhang, X. L., Zhou, H. G., Zhou, L. Y., Dong, F. and Shi, Q. F.: The influence of emission control on particle number size distribution and new particle formation during China's V-Day parade in 2015, Sci Total Environ, 573: 409-419, DOI: 10.1016/j.scitotenv.2016.08.085, 2016.

Shen, X. J., Sun, J. Y., Zhang, Y. M., Wehner, B., Nowak, A., Tuch, T., Zhang, X. C., Wang, T. T., Zhou, H. G., Zhang, X. L., Dong, F., Birmili, W. and Wiedensohler, A.: First long-term study of particle number size distributions and new particle formation events of regional aerosol in the North China Plain, Atmos. Chem. Phys., 11(4): 1565-1580, DOI: 10.5194/acp-11-1565-2011, 2011.

Sihto, S.-L., Kulmala, M., Kerminen, V.-M., Maso, M. D., Petäjä, T., Riipinen, I., Korhonen, H., Arnold, F., Janson, R., Boy, M., Laaksonen, A. and Lehtinen, K. E. J.: Atmospheric sulphuric acid and aerosol formation: implications from atmospheric measurements for nucleation and early growth mechanisms, Atmos. Chem. Phys., 6: 4079–4091, 2006.

Stolzenburg, D., Simon, M., Ranjithkumar, A., Kürten, A., Lehtipalo, K., Gordon, H., Ehrhart, S., Finkenzeller, H., Pichelstorfer, L., Nieminen, T., He, X.-C., Brilke, S., Xiao, M., Amorim, A., Baalbaki, R., Baccarini, A., Beck, L., Bräkling, S., Caudillo Murillo, L., Chen, D., Chu, B., Dada, L., Dias, A., Dommen, J., Duplissy, J., El Haddad, I., Fischer, L., Gonzalez Carracedo, L., Heinritzi, M., Kim, C., Koenig, T. K., Kong, W., Lamkaddam, H., Lee, C. P., Leiminger, M., Li, Z., Makhmutov, V., Manninen, H. E., Marie, G., Marten, R., Müller, T., Nie, W., Partoll, E., Petäjä, T., Pfeifer, J., Philippov, M., Rissanen, M. P., Rörup, B., Schobesberger, S., Schuchmann, S., Shen, J., Sipilä, M., Steiner, G., Stozhkov, Y., Tauber, C., Tham, Y. J., Tomé, A., Vazquez-Pufleau, M., Wagner, A. C., Wang, M., Wang, Y., Weber, S. K., Wimmer, D., Wlasits, P. J., Wu, Y., Ye, Q., Zauner-Wieczorek, M., Baltensperger, U., Carslaw, K. S., Curtius, J., Donahue, N. M., Flagan, R. C., Hansel, A., Kulmala, M., Lelieveld, J., Volkamer, R., Kirkby, J. and Winkler, P. M.: Enhanced growth rate of atmospheric particles from sulfuric acid, Atmos. Chem. Phys., 20(12): 7359-7372, DOI: 10.5194/acp-20-7359-2020, 2020.

Suni, T., Kulmala, M., Hirsikko, A., Bergman, T., Laakso, L., Aalto, P. P., Leuning, R., Cleugh, H., Zegelin, S., Hughes, D., Gorsel, E. v., Kitchen, M., Vana, M., H~orrak, U., Mirme, S., Mirme, A., Sevanto, S., Twining, J. and Tadros, C.: Formation and characteristics of ions and charged aerosol particles in a native Australian Eucalypt forest, Atmos. Chem. Phys, 8: 129–139, 2008.

Wang, H., Lu, K., Guo, S., Wu, Z., Shang, D., Tan, Z., Wang, Y., Le Breton, M., Lou, S., Tang, M., Wu, Y., Zhu, W., Zheng, J., Zeng, L., Hallquist, M., Hu, M. and Zhang, Y.: Efficient N_2O_5 uptake and NO_3 oxidation in the outflow of urban Beijing, Atmospheric Chemistry and Physics, 18(13): 9705-9721, DOI: 10.5194/acp-18-9705-2018, 2018.

Wang, X., Shen, X. J., Sun, J. Y., Zhang, X. Y., Wang, Y. Q., Zhang, Y. M., Wang, P., Xia, C., Qi, X. F. and Zhong, J. T.: Size-resolved hygroscopic behavior of atmospheric aerosols during heavy aerosol pollution episodes in Beijing in December 2016, Atmos. Environ., 194: 188-197, DOI: 10.1016/j.atmosenv.2018.09.041, 2018.

Wang, Y. Q., Zhang, X. Y. and Draxler, R. R.: TrajStat: GIS-based software that uses various trajectory statistical analysis methods to identify potential sources from long-term air pollution measurement data, Environmental Modelling & Software, 24(8): 938-939, DOI: 10.1016/j.envsoft.2009.01.004, 2009.

Wiedensohler, A., Cheng, Y. F., Nowak, A., Wehner, B., Achtert, P., Berghof, M., Birmili, W., Wu, Z. J., Hu, M., Zhu, T., Takegawa, N., Kita, K., Kondo, Y., Lou, S. R., Hofzumahaus, A., Holland, F., Wahner, A., Gunthe, S. S., Rose, D., Su, H. and Pöschl, U.: Rapid aerosol particle growth and increase of cloud condensation nucleus activity by secondary aerosol formation and condensation: A case study for regional air pollution in northeastern China, J. Geophys. Res., 114, DOI:

10.1029/2008jd010884, 2009.

505   Yan, C., Nie, W., Äijälä, M., Rissanen, M. P., Canagaratna, M. R., Massoli, P., Junninen, H., Jokinen, T., Sarnela, N., Häme, S. A. K., Schobesberger, S., Canonaco, F., Yao, L., Prévôt, A. S. H., Petäjä, T., Kulmala, M., Sipilä, M., Worsnop, D. R. and Ehn, M.: Source characterization of highly oxidized multifunctional compounds in a boreal forest environment using positive matrix factorization, Atmospheric Chemistry and Physics, 16(19): 12715-12731, DOI: 10.5194/acp-16-12715-2016, 2016.

Yan, C., Nie, W., Vogel, A. L., Dada, L., Lehtipalo, K., Stolzenburg, D., Wagner, R., Rissanen, M. P., Xiao, M., Ahonen, L.,
510   Fischer, L., Rose, C., Bianchi, F., Gordon, H., Simon, M. and Heinritzi, M.: Size-dependent influence of NOx on the growth rates of organic aerosol particles, Science Advance, 6: eaay4945, 2020.

Yu, F. and Turco, R.: Case studies of particle formation events observed in boreal forests: implications for nucleation mechanisms, Atmos. Chem. Phys., 8: 6085–6102, 2008.

Yu, F. and Turco, R. P.: The size-dependent charge fraction of sub-3-nm particles as a key diagnostic of competitive nucleation
515   mechanisms under atmospheric conditions, Atmos. Chem. Phys., 11(18): 9451-9463, DOI: 10.5194/acp-11-9451-2011, 2011.

Yu, F. Q. and Turco, R. P.: Ultrafine aerosol formation via ion-mediated nucleation, Geophys. Res. Lett., 27(6): 883-886, DOI: 10.1029/1999gl011151, 2000.

Yuan, B., Koss, A. R., Warneke, C., Coggon, M., Sekimoto, K. and de Gouw, J. A.: Proton-Transfer-Reaction Mass Spectrometry: Applications in Atmospheric Sciences, Chemical Reviews, 117(21): 13187-13229, DOI:
520   10.1021/acs.chemrev.7b00325, 2017.

Zhang, Q., Pan, Y., He, Y., Walters, W. W., Ni, Q., Liu, X., Xu, G., Shao, J. and Jiang, C.: Substantial nitrogen oxides emission reduction from China due to COVID-19 and its impact on surface ozone and aerosol pollution, Sci Total Environ, 753, DOI: 10.1016/j.scitotenv.2020.142238, 2021.

Zhang, X. Y., Xu, X. D., Ding, Y. H., Liu, Y. J., Zhang, H. D., Wang, Y. Q. and Zhong, J. T.: The impact of meteorological
525   changes from 2013 to 2017 on PM2.5 mass reduction in key regions in China, Science China Earth Sciences, 62(12): 1885–1902, 2019.

Zhong, J., Zhang, X., Dong, Y., Wang, Y., Liu, C., Wang, J., Zhang, Y. and Che, H.: Feedback effects of boundary-layer meteorological factors on cumulative explosive growth of PM2.5 during winter heavy pollution episodes in Beijing from 2013 to 2016, Atmospheric Chemistry and Physics, 18(1): 247-258, DOI: 10.5194/acp-18-247-2018, 2018.

530

Table 1. Parameters characterizing NPF events during ~~pre~~Pre-_LCD, LCD, and ~~post~~Post-_LCD, including NPF frequency, formation rate ($J_{2,par}$, J_{2,pos_ion}, J_{2,neg_ion}) and growth rate ($GR_{2,par}$, GR_{pos_ion}, GR_{neg_ion}) of the total particles and charge ions, as well as condensation sink (CS).

	Pre-LCD	LCD	Post-LCD
NPF ~~frequency~~event (available days)	~~43%~~10 (23)	~~33%~~~~9~~10 (24)	~~38%~~5 (13)
$J_{2,par}$ (cm^{-3}s^{-1})	5.6 ± 2.3	7.9 ± 4.5	5.9 ± 3.5
J_{2,pos_ion} (cm^{-3}s^{-1})	0.010 ± 0.003	0.032 ± 0.003	0.021 ± 0.014
J_{2,neg_ion} (cm^{-3}s^{-1})	0.009 ± 0.004	0.024 ± 0.005	0.015 ± 0.011
GR_{par} (nm h^{-1})	0.8 ± 0.5	1.5 ± 0.7	2.0 ± 0.5
GR_{pos_ion} (nm h^{-1})	1.8 ± 0.3	3.1 ± 0.2	3.6 ± 0.4
GR_{neg_ion} (nm h^{-1})	2.0 ± 0.7	3.1 ± 0.4	3.2 ± 0.4
CS (s^{-1})	0.010 ± 0.003	0.008 ± 0.006	0.008 ± 0.003

535
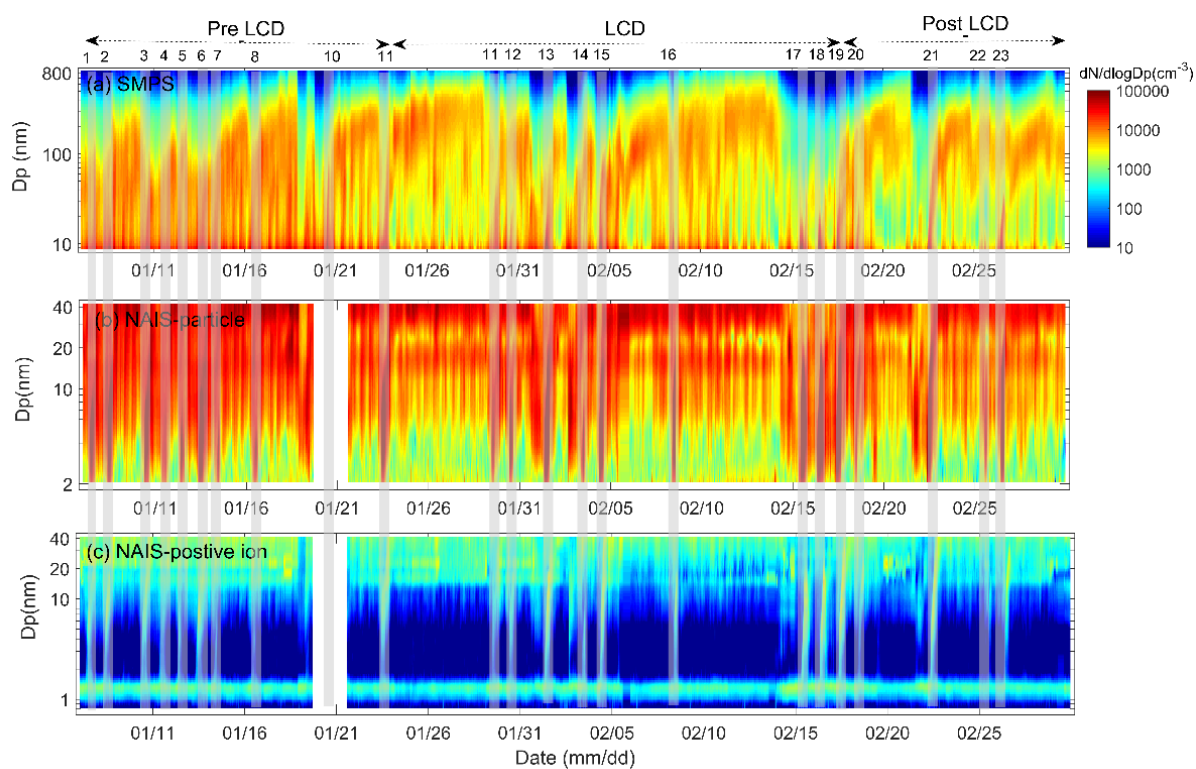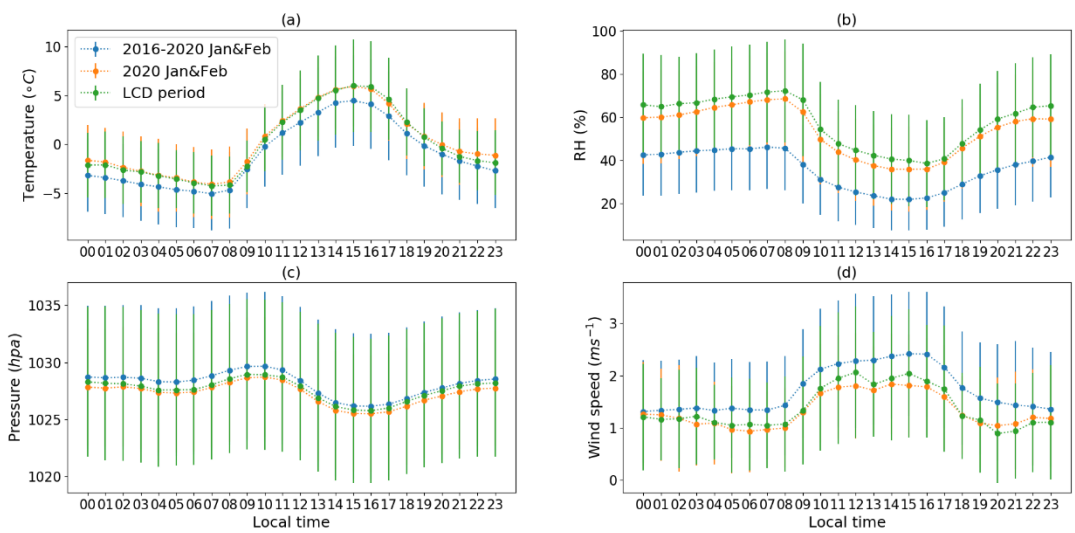
Fig. 1. The mean diurnal pattern of meteorological parameters, including temperature (a), RH (b), sea level pressure (c) and wind speed (d) during LCD period (January 24-February 16, 2020), January and February in 2020 and in 2016-2020. The solid circles and bars represent the mean value and the standard deviation, respectively.
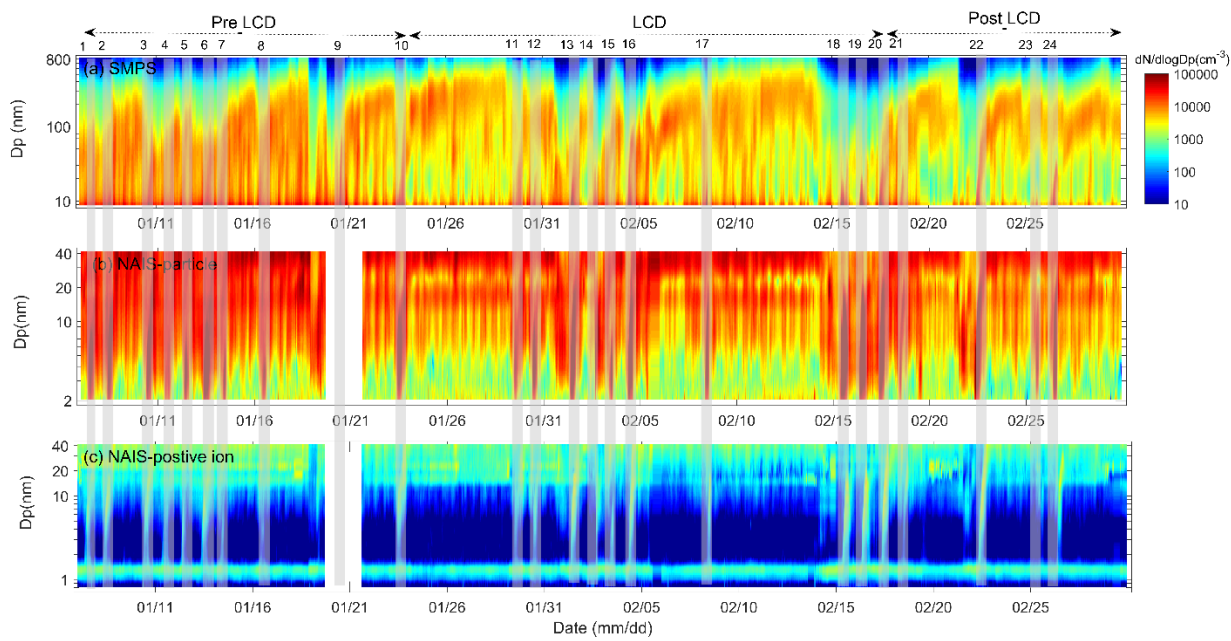
20
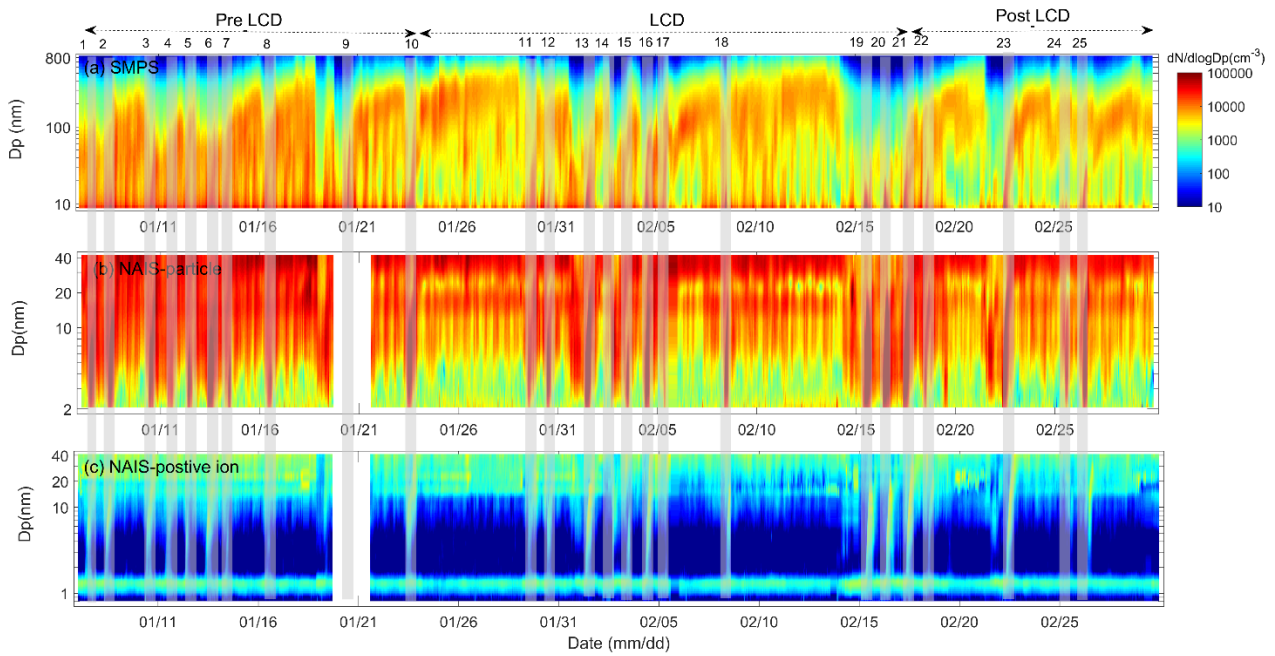
Fig. ~~1~~2. Time evolution of number size distribution of 10–850 nm particles by SMPS (a), neutral 2–42 nm particles by NAIS

in positive particle mode (b), and positive 0.8–42 nm ions by NAIS (c). NPF events were marked by numbers from 1–~~23~~25.
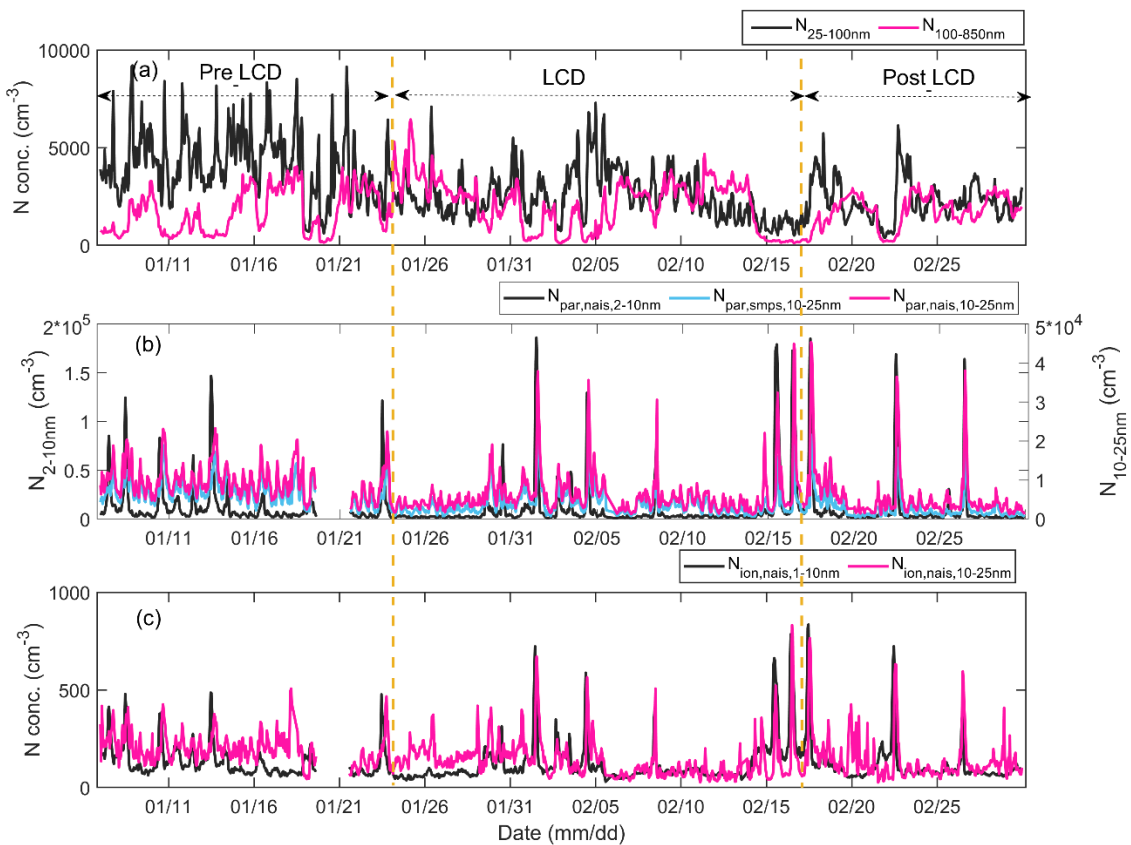
Fig. ~~2~~3. Time series of hourly mean of the number concentrations for different size ranges, including 25–100 nm and

100–850 nm, from SMPS data (a); 2–10 nm particles from NAIS and 10–25 nm particles from both NAIS and SMPS

(b); 1–10 nm and 10–25 nm positive ions from NAIS (c).
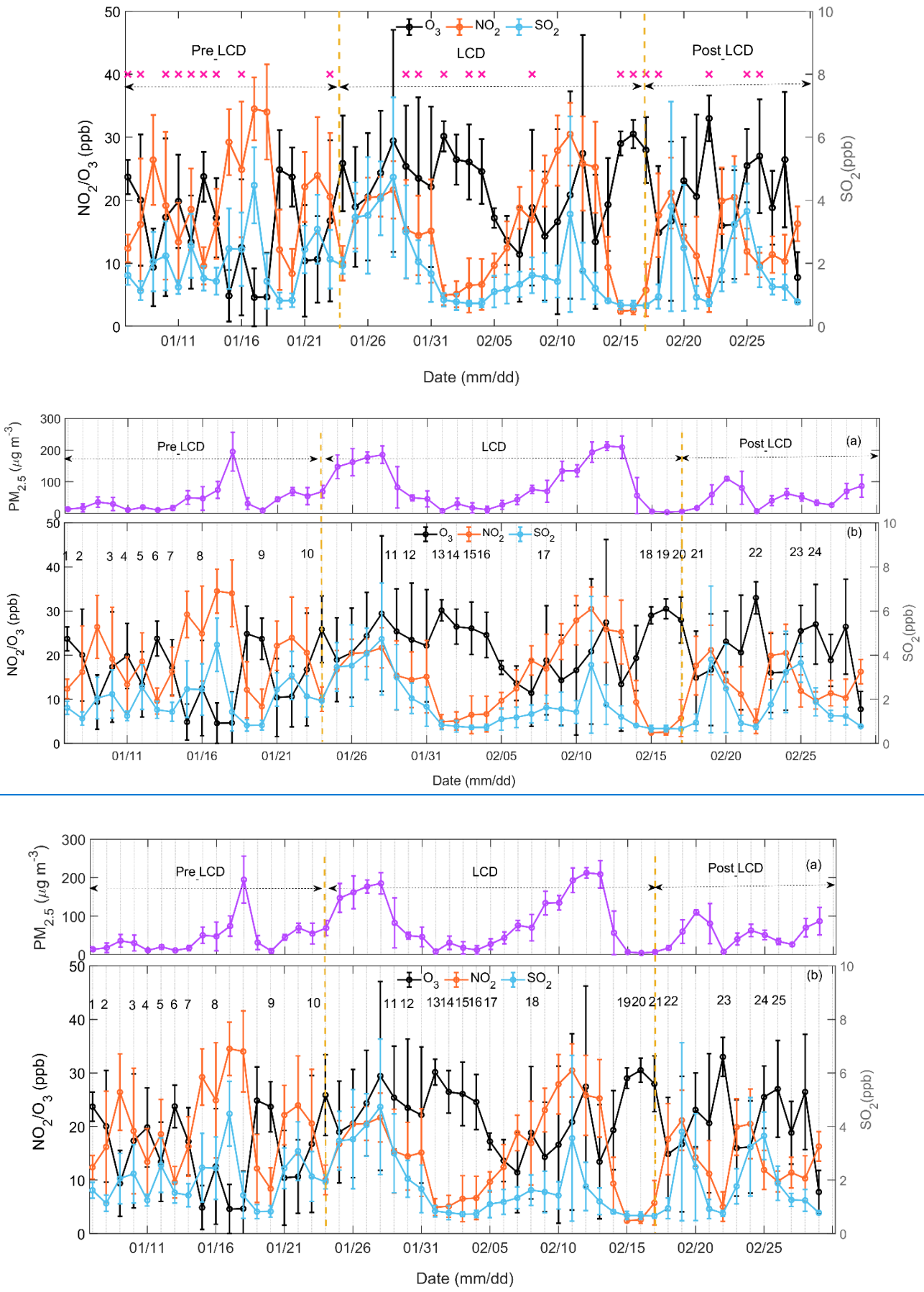
Fig. 34. Concentration level of PM$_{2.5}$ mass concentration (a), and precursors (b), including NO$_2$ (a), SO$_2$ (b), and O$_3$ (c)

during the measurement period. The circle and bar indicate the mean and standard deviation, respectively; NPF days are

marked with ~~a pink cross~~continuous numbers 1-2~~4~~5.
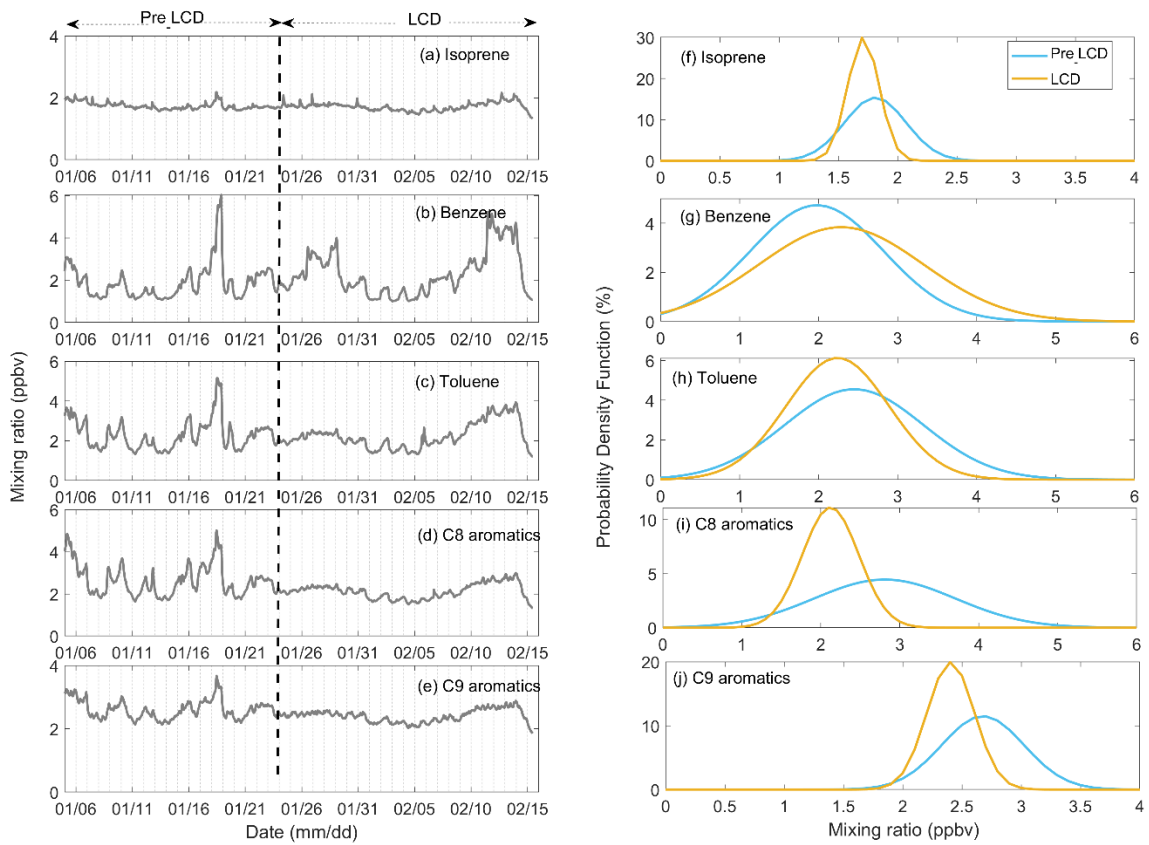

Fig. 5. Time series of isoprene, benzene, toluene, C8 and C9 aromatics (a-e) during January 5 to February 15, and the probability distribution function of mixing ration of each VOC component (f-j), respectively.
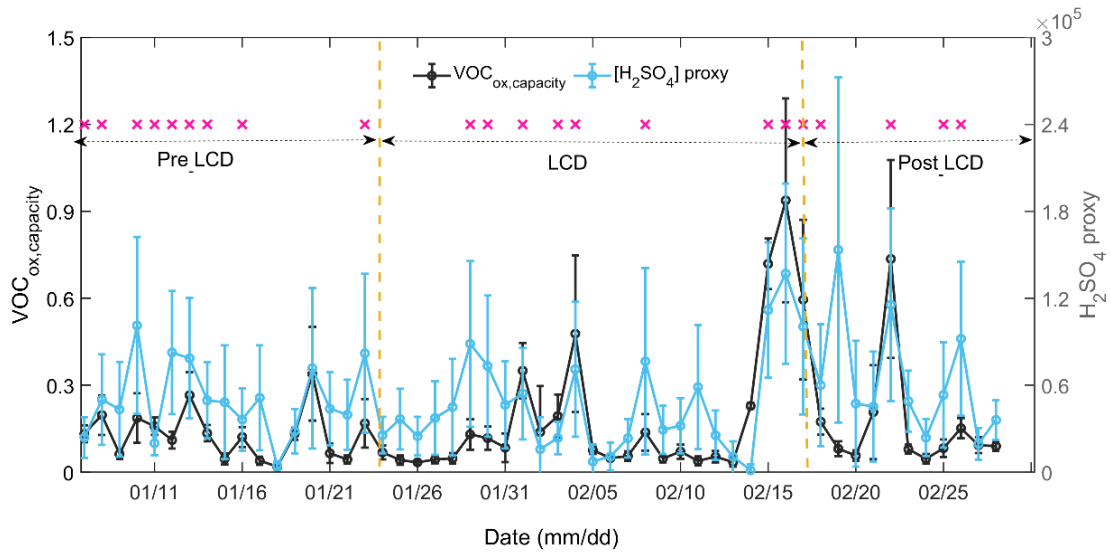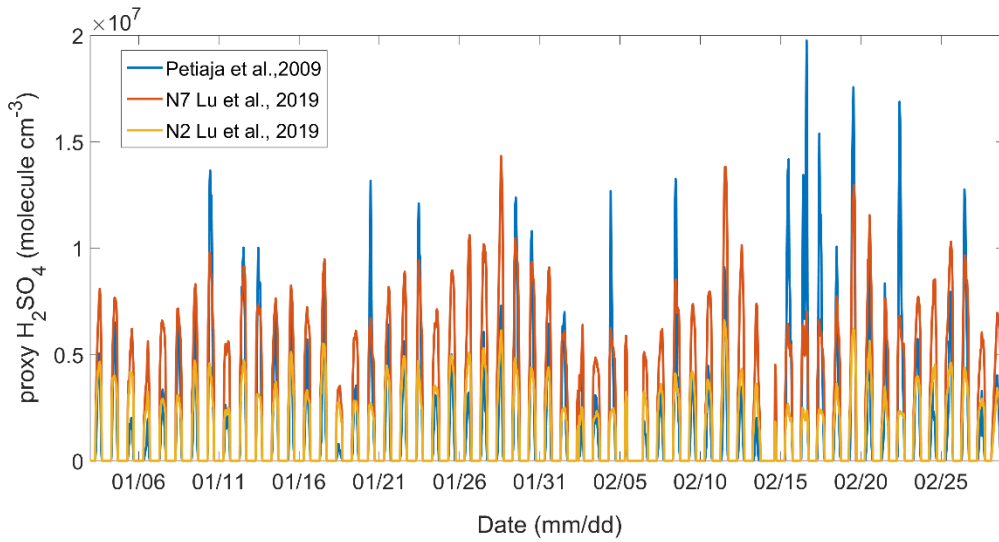
Fig. 46. The sulfuric acid concentrations derived by different proxy equations. The red and orange lines indicate the result by N2 and N7 method by Lu et al. (2019), and blue line indicates the method recommend by Petiäjä et al. (2009). ~~Estimated oxidized capacity of the VOC (VOCox, capacity) and sulfuric acid proxy (H₂SO₄) during pre-LCD, LCD and post-LCD, respectively. The circle and bar indicate the mean and standard deviation, respectively; NPF days are marked with a pink cross.~~
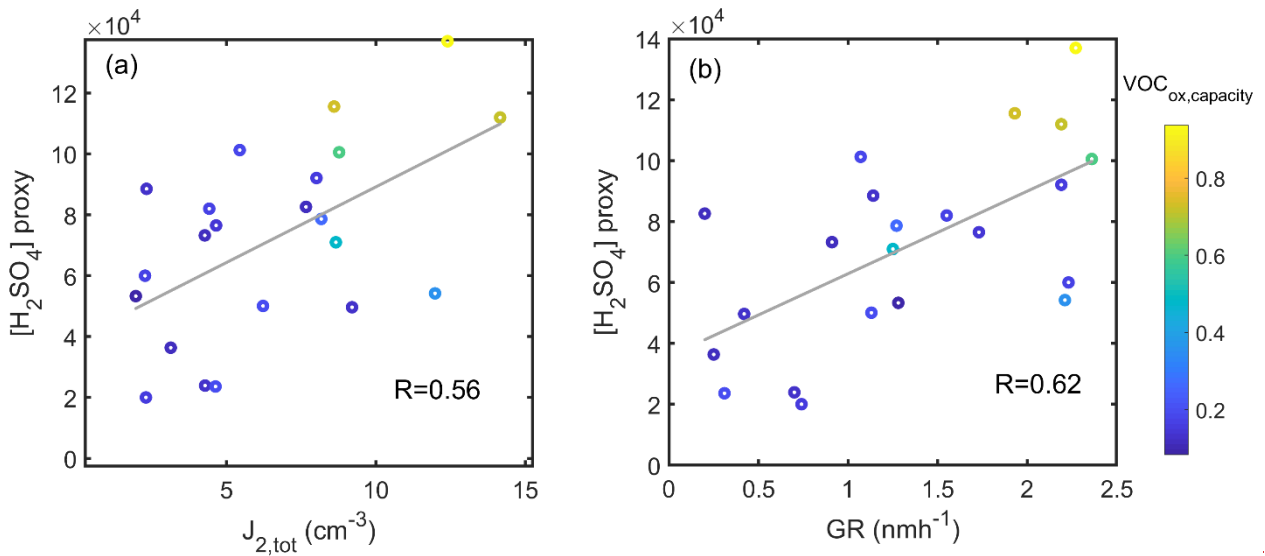
~~Fig. 5. Scatter plot of *J* (a) and *GR* (b) versus the proxy of sulfuric acid and VOC oxidization~~ oxidizing capacity ~~(VOCox,capicity) for all NPF events. The color of the circles indicates the level of VOCox,capacity. The linear fit lines (gray) and correlation coefficient (*R*) are given.~~
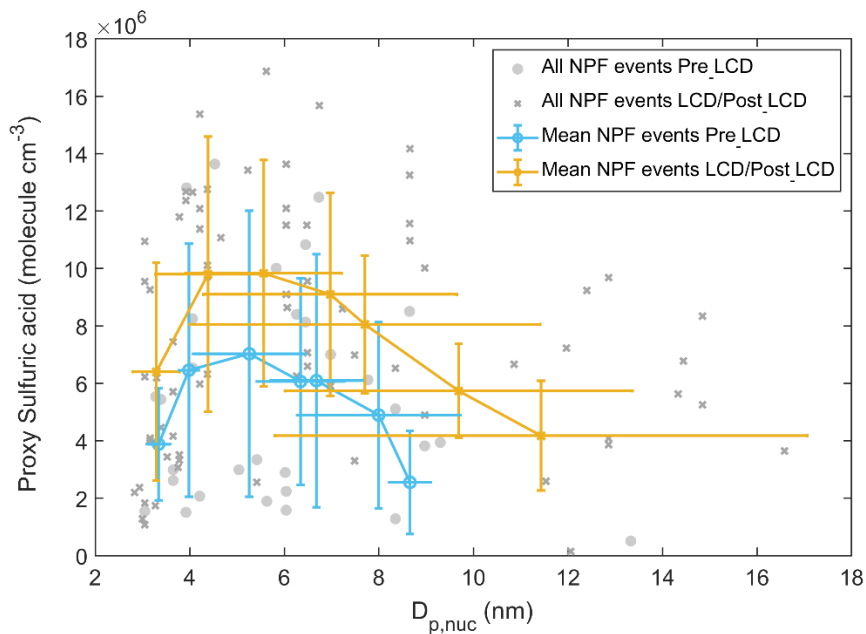
Fig. 7. Scatter plot between geometric mean diameter of nucleation mode ($D_{p,nuc}$) and the proxy sulfuric acid. The grey dots and crosses represent the NPF events during Pre_LCD, LCD/Post_LCD, respectively. The purple and blue lines represent the mean conditions during Pre_LCD, LCD/Post_LCD. The vertical and horizontal bars represents the standard deviations of sulfuric acid and $D_{p,nuc}$.
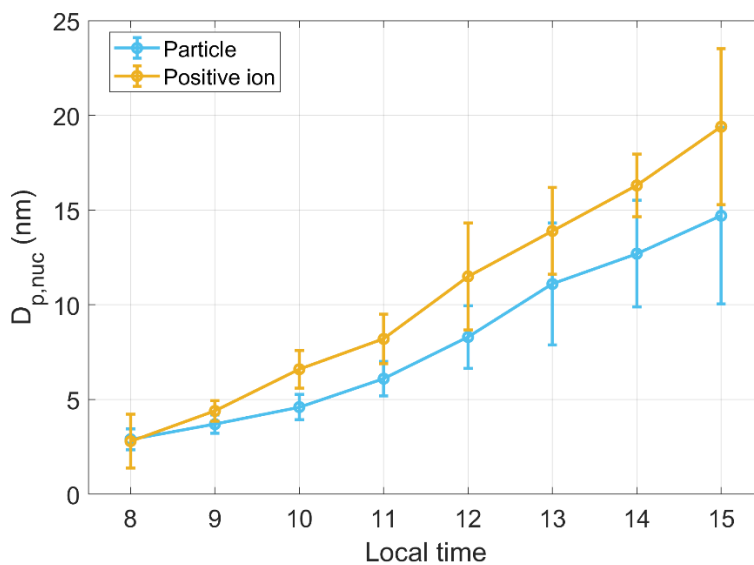
Fig. 8. The time evolution of geometric mean diameter of nucleation mode ($D_{p,nuc}$) of neutral particle and positive charged ions during the NPF events. The circle and bar present the mean value and the standard deviation.
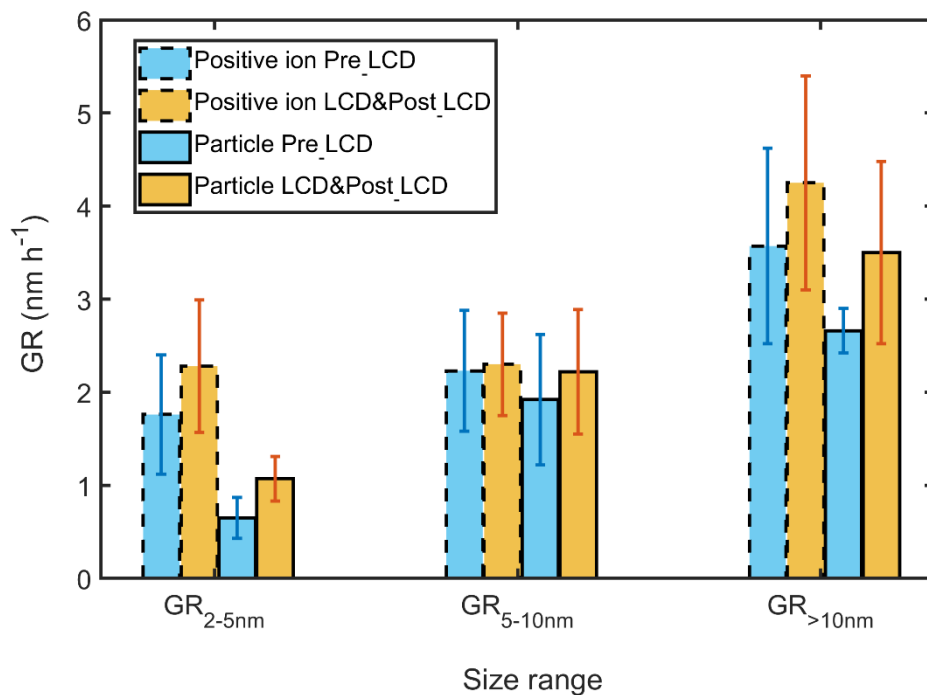
25

Fig. ~~6~~9. The mean values of ~~g~~Growth rates of particles and ions in different size ranges, including 2–5 nm ($GR_{2–5nm}$), 5–10 nm ($GR_{5–10nm}$), and >10 nm ($GR_{>10nm}$), during Pre_LCD and LCD&Post_LCD, respectively. The histogram and error bars represent the mean value and standard deviation, respectively.
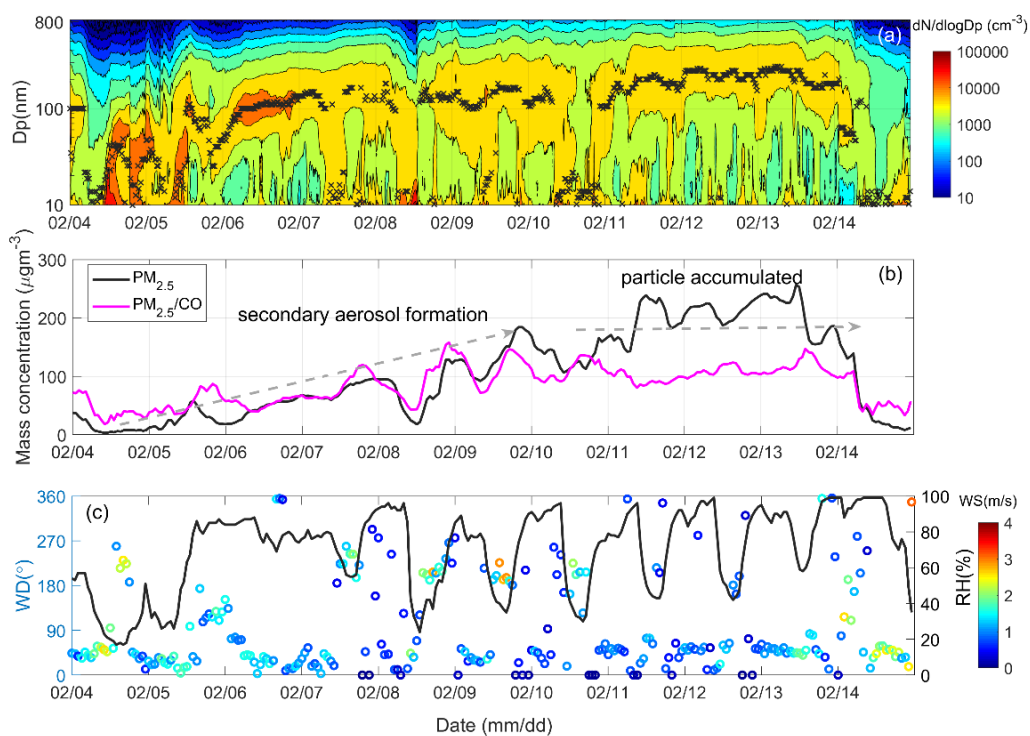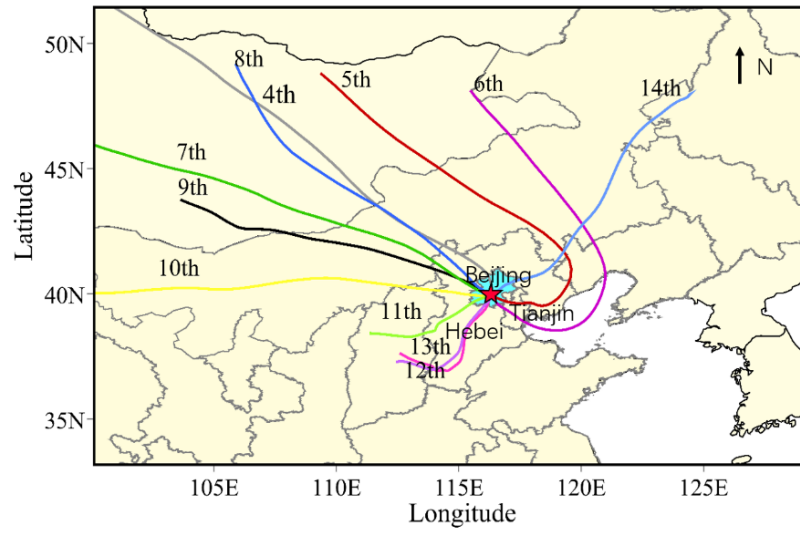

Fig. ~~7~~10. Time evolution of PNSD and the dominant geometric mean diameters (black cross) derived by the log-modal fitting (a) and hourly mean $PM_{2.5}$ (black line), normalized $PM_{2.5}$ by CO (pink line) in (b) and the meteorological factors: wind direction (WD), wind speed (WS), and relative humidity (RH, black line) in (c) on February 4–14.

26

Fig. 811. The back trajectories arriving at CAMS station at 12:00 local time form February 4 to 14 with the terminal height of 500 m agl.